ACS OMEGA

Open Access

http://pubs.acs.org/journal/acsodf

Article

Effects of Inhomogeneous Gas Diffusion Layer Properties on the Transportation Phenomenon and Performances of Proton-Exchange Membrane Fuel Cells

Hangwei Lei, Yuzhen Xia, and Guilin Hu*

Cite This: *ACS Omega* 2024, 9, 9383−9395

Read Online

ACCESS | Metrics & More | Article Recommendations

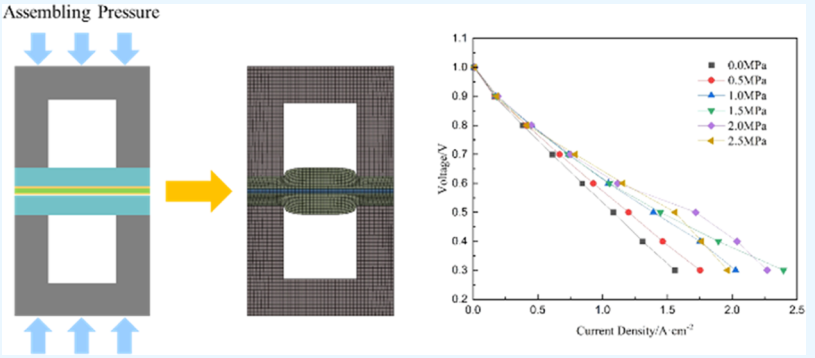

ABSTRACT: The encapsulation of the proton-exchange membrane fuel cell (PEMFC) is an essential step of fuel cell stack assembly. The selection of the assembly pressure is very important to the stack performance and life. Based on that, this paper presents a method to describe the internal physical deformation of the gas diffusion layer (GDL) after inhomogeneous pressure by using user-defined functions (UDFs). The results show that the transmission difference caused by the nonuniform GDL deformation can be clearly seen by the UDFs method, and there is an obvious transition of GDL at the interface of the channel and the rib. A three-dimensional single-channel PEMFC model is established, and an optimal assembly pressure range is obtained, between 1.5 and 2.0 MPa. The maximum thermal stress inside the cell occurs in the middle of the membrane electrode assembly and decreases as the assembly pressure increases. Furthermore, the influence of rib−channel ratios is discussed. Compared to the fuel cells with ratios of 2:1, 2:3, and 1:2, the one with 1:1 exhibits the maximum current density and the highest power density.

1. INTRODUCTION

With the development of industry, the issues of resource depletion and environmental problems have become more and more serious. Clean and efficient energy utilization methods are gradually becoming the mainstream direction for future energy development and utilization. A proton-exchange membrane fuel cell (PEMFC) has been considered a very strong competitor for the power sources of future vehicles for its advantages, such as high energy utilization, low or zero emission, and short startup time.[1−4]

In order to further understand the mechanisms and improve fuel cell systems, many researchers have engaged in modeling and computer simulation studies of PEMFC. In terms of its developmental journey, the models have evolved from simple one-dimensional single-channel mathematical models to complex three-dimensional cell stack models.[5−7] Furthermore, the characteristics being studied by the models have become increasingly complex, ranging from single-phase flow to multiphase flow,[8,9] from steady-state simulations to transient simulations,[10,11] and from macroscopic cell models to the establishment of mathematical models within the gas diffusion layer (GDL)[12,13] and the catalyst layer (CL)[14,15] at the micro and mesoscale. In particular, pore-scale models based on the Lattice Boltzmann method gained significant attention for their capability to elucidate the transport processes of water within the GDL at the micro and mesoscales.[16,17] However, the aforementioned mathematical models established through numerical simulations have not considered the deformation of the GDL caused by assembly pressure, as well as the resulting changes in the GDL's physical properties, internal temperature,

Received: November 4, 2023
Revised: January 16, 2024
Accepted: January 23, 2024
Published: February 12, 2024

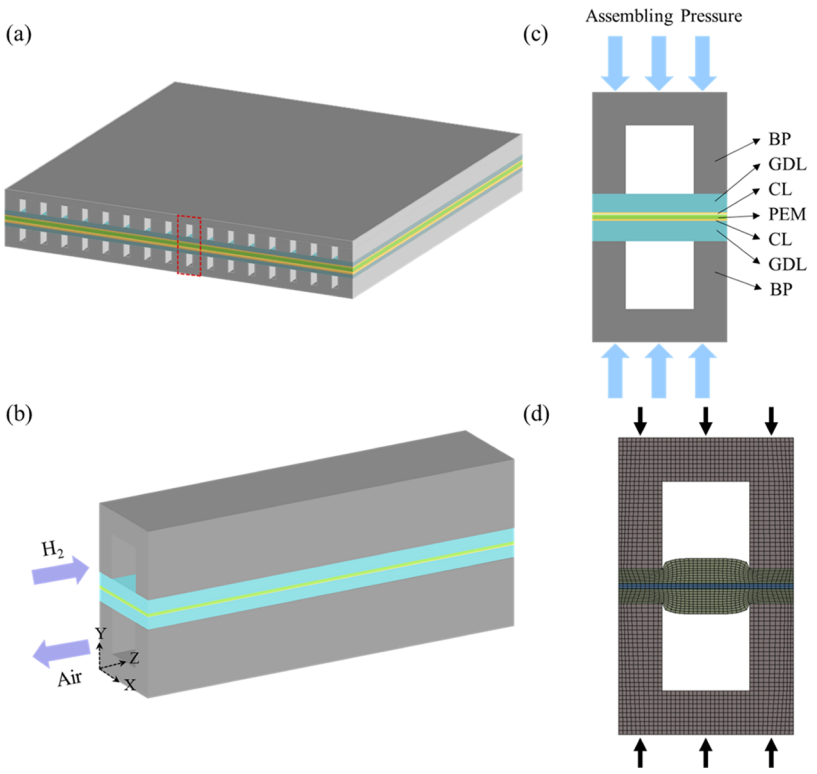

Figure 1. PEMFC model and computation domain, (a) single cell model, (b) single-channel cell model, (c) assembly pressure and cell parts schematic, and (d) grid diagram of the *XY* cross section after compression deformation.

and thermal stress distribution and their impact on cell performance.

Therefore, the selection of fuel cell assembly pressure and detailed theoretical research have become increasingly important. The choice of assembly load is crucial for the performance and lifespan design of fuel cell stacks.[18] Since GDL has the worst mechanical properties among all components, it is the component that undergoes major deformation during assembly. Therefore, some researchers have studied the performance of the GDL after deformation. Zhou et al.[19] studied the effects of compression and different parameters (carbon fiber diameter, porosity) on two-phase flow in GDL using a fluid volume method. The results showed that the larger the fiber diameter and porosity, the more favorable the water transport. Zhang et al.[20] utilized the finite element method (FEM) to investigate the compressive deformation of GDL from a microscopic perspective. The results demonstrated that different porosities, fiber diameters, and thicknesses lead to varied microstructure effects on GDL deformation. With increasing pressure, the porosity decreases. Chen et al.[21] examined the impact of assembly pressure on the mechanical properties of commercial carbon paper-based GDL. The study revealed that excessive assembly stress can lead to carbon fiber breakage, affecting its transport performance. It was also found that the spatial arrangement of pores with a diameter below 0.175 nm was largely unaffected, while it did have an influence on the spatial arrangement of larger pores with a diameter exceeding 0.2 nm. These are studies on the physical properties and mechanical strength of GDL after deformation, and the influence of GDL deformation on internal transmission and cell performance is not studied. Because the deformation of the cell model is complex under various assembly pressures, many researchers have studied it by simplifying the model. Chi et al.[22] assumed that the physical characteristics of GDL in the compressed flow channel were uniform, and the deformation of GDL was not considered. By taking the average value of the physical parameters of the compressed GDL, a numerical simulation was carried out. Su et al.[23] established a nonuniform deformation GDL, but the model ignored the deformation at the junction of the channel and the rib and treated the GDL inside the channel as the thickness. It was found that this model is superior to the uniform GDL model. Chippar et al.[24] subdivided the uniform and nonuniform GDL models into three working conditions: uncompressed GDL, uninvaded GDL, and invaded GDL. The results showed that nonuniform GDL compression and intrusion had a significant effect on PEMFC internal transport properties. All of the above studies simplify the GDL deformation model and do not consider the transition of the junction position of the rib and the channel, as well as the nonuniform distribution of the physical parameters. Some studies focus on the influence of different working conditions and materials on the performance of GDL cells after compression deformation. Shrivastava et al.[25] conducted experimental research on the influence of different gas humidity levels and compression ratios on the performance of PEMFC. The experiments revealed that the performance initially improves and then deteriorates with increasing pressure. In their study, the best performance of the cell was achieved at a compression ratio of 14.2 and 25.7% at 100 and 50% gas humidity, respectively. Movahedi et al.[26] studied the effect of assembly pressure on the performance of cells with GDL thicknesses. The study found that the optimal assembly pressures for GDL thicknesses of 110, 254, and 370 μm were determined to be 0.395, 0.696, and 1.101 MPa, respectively. Kang et al.[27] developed a two-dimensional FEM of the stacked metal bipolar plate (BP) to examine the phenomenon of stress

https://doi.org/10.1021/acsomega.3c08756
ACS Omega 2024, 9, 9383−9395

concentration in the membrane electrode assembly (MEA) under assembly pressure. The consequences indicated that stress significantly concentrates in the membrane region beneath the rib edges of BP, potentially causing plastic deformation of the membrane. The aforementioned works mainly focused on mass transport and cell performance due to GDL deformation but did not consider the thermal stress and temperature distribution within the compressed cell. The internal temperature and thermal stress distribution during fuel cell operation play crucial roles in its performance and lifespan.

Therefore, this paper considers the nonuniform GDL deformation and proposes a method using UDFs to set the nonuniform porosity and permeability of GDL after deformation. At the same time, this paper explores mass transport, temperature distribution, thermal stress, mechanical stress, and cell performance under different assembly pressures and observes that the optimal assembly pressure varies between low-voltage and intermediate-voltage conditions. Moreover, the impact of rib−channel ratios on the distribution of current density and cell performances at 1.5 and 2.0 MPa are studied.

2. MODEL DEVELOPMENT

2.1. Model Assumptions. The following assumptions are considered to develop the simplified mathematical model for PEMFC:

(1) The fuel cell is in the steady operation state.
(2) Except for GDL, other materials are isotropic and homogeneous porous media.
(3) Except for GDL, other components of PEMFC do not deform under various assembly pressures.
(4) All gases are ideal gases, and the fluid flow is laminar.
(5) The contact thermal resistance of the interface between GDL and BP is not taken into account

2.2. Geometric Model. Figure 1a shows a single PEMFC model. One single channel shown in Figure 1b is selected as the computation domain for saving the computation time. The fuel cell model is composed of BP, GDL, CL, and PEM, as illustrated in Figure 1c, whose dimensions are given in Table 1. The fuel cell model and its meshes with deformed GDL for the compression are illustrated in Figure 1d.

2.3. Stress−Strain Model for GDL. To calculate the deformation of GDL, the equations representing the connection between stress, strain, and external load are described as follows, which are similar to our previous work.[29]

The force balance for the GDL is written as eq 1.

$$\begin{cases} F_x + \dfrac{\partial \sigma_x}{\partial x} + \dfrac{\partial \tau_{yx}}{\partial y} + \dfrac{\partial \tau_{zx}}{\partial z} = 0 \\ F_y + \dfrac{\partial \sigma_y}{\partial y} + \dfrac{\partial \tau_{zy}}{\partial z} + \dfrac{\partial \tau_{xy}}{\partial x} = 0 \\ F_z + \dfrac{\partial \sigma_z}{\partial z} + \dfrac{\partial \tau_{xz}}{\partial x} + \dfrac{\partial \tau_{yz}}{\partial y} = 0 \end{cases} \tag{1}$$

where F_x, F_y, and F_z are the body forces in the x-, y-, and z-directions, respectively; σ_x, σ_y, and σ_z are the positive stresses in the corresponding directions (Pa); and τ_{xy}, τ_{yz}, and τ_{zx} are the shear stresses at the xy-, yz-, and zx-planes, respectively (Pa).

The deformation and strains of GDL relate to the displacements as in eq 2.

$$\begin{cases} \psi_x = \dfrac{\partial u}{\partial x},\ \psi_{xy} = \dfrac{1}{2}\left(\dfrac{\partial u}{\partial y} + \dfrac{\partial v}{\partial x}\right) \\ \psi_y = \dfrac{\partial v}{\partial y},\ \psi_{yz} = \dfrac{1}{2}\left(\dfrac{\partial v}{\partial z} + \dfrac{\partial w}{\partial y}\right) \\ \psi_z = \dfrac{\partial w}{\partial z},\ \psi_{zx} = \dfrac{1}{2}\left(\dfrac{\partial w}{\partial x} + \dfrac{\partial u}{\partial z}\right) \end{cases} \tag{2}$$

where ψ_x, ψ_y, and ψ_z are positive strains in x-, y-, and z-directions; u, v, and w are displacements in the corresponding directions; and ψ_{xy}, ψ_{yz}, and ψ_{zx} are shear strains at the xy-, yz-, and zx-planes, respectively.

The strain or deformation is physically related to stress by eq 3.

$$\begin{cases} \psi_x = \dfrac{\sigma_x - \mu(\sigma_y + \sigma_z)}{E} \\ \psi_y = \dfrac{\sigma_y - \mu(\sigma_z + \sigma_x)}{E} \\ \psi_z = \dfrac{\sigma_z - \mu(\sigma_x + \sigma_y)}{E} \end{cases} \tag{3}$$

where E is the elastic modulus (Pa) and μ is the porosity of GDL.

2.4. PEMFC Model Based on CFD. The numerical simulation of the transportation phenomenon in PEMFC is based on a 3D CFD model considering geometric deformation. The conservation equations of the PEMFC mathematical model include heat/mass transfer, momentum, and charge transport. The conservation equations of the simplified model for mass, momentum, temperature, species, and charges are written as eqs 4−8.

$$\nabla\cdot(\varepsilon\rho u) = S_{\mathrm{m}} \tag{4}$$

$$\nabla\cdot(\varepsilon\rho \boldsymbol{uu}) = -\varepsilon\nabla p + \nabla\cdot(\varepsilon\mu\nabla u) + S_{\mathrm{u}} \tag{5}$$

$$\nabla\cdot(\varepsilon\rho c_{\mathrm{p}} uT) = \nabla\cdot(\lambda^{\mathrm{eff}}\nabla T) + S_{\mathrm{Q}} \tag{6}$$

$$\nabla\cdot(\varepsilon u c_{\mathrm{i}}) = \nabla\cdot(D_{\mathrm{i}}^{\mathrm{eff}}\nabla c_{\mathrm{i}}) + S_{\mathrm{i}} \tag{7}$$

$$\nabla\cdot(\gamma_{\mathrm{j}}^{\mathrm{eff}}\nabla\phi_{\mathrm{j}}) = S_{\phi\mathrm{j}} \tag{8}$$

where ε is the porosity of different components, which equals zero for BP and unit for channel; $\boldsymbol{u}$ represents the intrinsic velocity (m·s^{-1}), which is zero in BP; ρ is the fluid density (kg·

Table 1. Some Basic Parameters and Working Conditions

parameters	values
channel width/height (mm)	1/1
rib width (mm)	0.5
BP width/length/height (mm)	2/50/1.5
primary GDL thickness (mm)	0.28
membrane thickness (mm)	0.05
CL thickness (mm)	0.01
working temperature (K)	353.13
working pressure (Pa)	101 325
anode stoichiometry ratio	1.5
cathode stoichiometry ratio	2
open circuit voltage (V)	1.1
Faraday constant (C·mol^{-1})	96 485
primary contact electric resistance (mΩ·cm^2)	14.3[28]

https://doi.org/10.1021/acsomega.3c08756
ACS Omega 2024, 9, 9383−9395

m^{-3}); μ is the dynamic viscosity of fluid ($kg{\cdot}m^{-1}{\cdot}s^{-1}$); p is fluid pressure (Pa); c_p is the specific heat capacity of the fluid ($J{\cdot}kg^{-1}{\cdot}K^{-1}$); λ stands for thermal conductivity ($W{\cdot}m^{-1}{\cdot}K^{-1}$); c_i is the species concentration; D_i^{effis} is the diffusion coefficient of species i ($m^2{\cdot}s^{-1}$); γ represents the electric conductivity ($S{\cdot}cm^{-1}$); φ is the potential (V), subscript j = s or m represents the solid phase and membrane phase, respectively; superscript eff indicates effective value; and S means source terms for mass, energy, momentum, species, and charges.

S_m is the mass source term, which indicates the total mass change for the electrochemical reaction as eq 9.

$$S_m = \begin{cases} S_{H_2} & \text{in the anode CL} \\ S_{O_2} + S_{H_2O} & \text{in the cathode CL} \\ 0 & \text{other components} \end{cases} \quad (9)$$

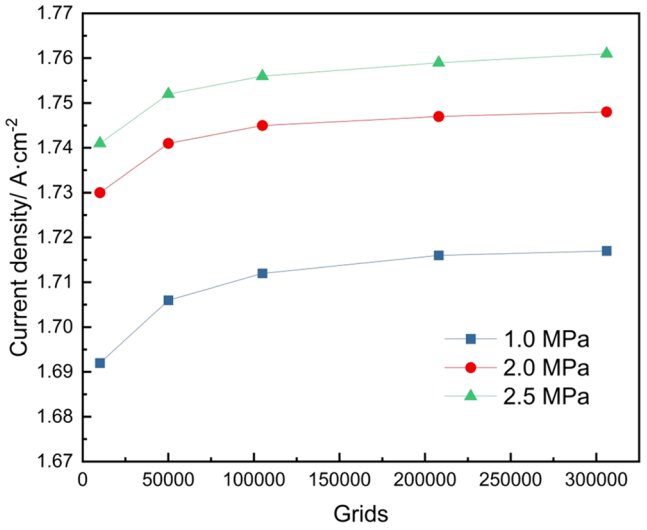

Figure 2. Numerical experiments on grid number independence.

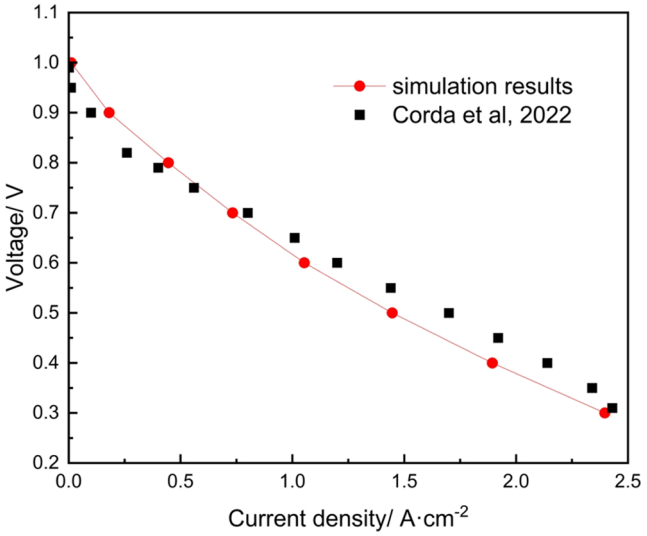

Figure 3. Comparison between the simulated and experimental performance

The source term S_u of the momentum equation is zero in other components except in GDL and CL for the interaction force between fluid and solid base in the porous media as eq 10.

$$S_u = \begin{cases} 0 & \text{other components} \\ \frac{\mu^{eff}}{K}\varepsilon\varepsilon u + \beta_2\frac{1}{2}\rho|\varepsilon u|\varepsilon u & \text{GDL and CL} \end{cases} \quad (10)$$

where K is the permeability (m^2) and β_2 represents the inertial resistance factor. The velocity in GDL and CL is normally low; the second-term inertia force is much lower than the first-term viscous force.

Considering the ohm heat of current for the membrane with high resistance, reversible, and irreversible reaction heat for CL, the source term S_Q for the energy conservation equation can be described as eq 11.

$$S_Q = \begin{cases} 0 & \text{fluid channel and GDL} \\ I \times A_{cv} \times \left(\frac{-T\Delta S}{nF} + \eta\right) & \text{CL} \\ I^2\gamma_{mem} & \text{PEM} \end{cases} \quad (11)$$

where I is the current density ($A{\cdot}cm^{-2}$), A_{cv} represents the specific surface area (m^{-1}), ΔS stands for the entropy change of electrochemical reaction, η means the activation over potential (V), and F is the Faraday constant ($C{\cdot}mol^{-1}$).

The gas species source terms S_i are not zero in CL for the electrochemical reaction, which can be described as following via Faraday's law as eq 12.

$$S_i = \begin{cases} -\frac{M_{H_2}}{2}|R_a| & \text{CL at anode} \\ -\frac{M_{O_2}}{4}|R_c| & \text{CL at cathode} \\ \frac{M_w}{2}|R_c| & \text{CL at cathode} \end{cases} \quad (12)$$

where M represents the molecular weight and R stands for electrochemical reaction rate. The electrochemical reaction rate can be defined by the Butler–Volmer equation (13).[31]

$$R_d = \frac{A_{cv,d}i_j^{ref}}{F}\left(\frac{C_j}{C_j^{ref}}\right)\varepsilon_{N,d}\left(e^{\alpha_a F\eta_d/RT} - e^{-\alpha_c F\eta_d/RT}\right) \quad (13)$$

where d stands for a or c for anode or cathode, respectively; i_j^{ref} is the reference exchange current density ($A{\cdot}cm^{-2}$), C_j^{ref} is the reference species concentration, and α represents the charge transfer coefficient ($W{\cdot}m^2{\cdot}K^{-1}$).

According to the electric neutrality, the source terms for electric potential and membrane potential in anode and cathode CL are equal with opposite symbols as in eqs 14 and 15

$$S_{\phi s} = \begin{cases} -R_a & \text{anode CL} \\ R_c & \text{cathode CL} \end{cases} \quad (14)$$

$$S_{\phi m} = \begin{cases} R_a & \text{anode CL} \\ -R_c & \text{cathode CL} \end{cases} \quad (15)$$

2.5. Numerical Procedures and Boundary Conditions.

The stress–strain model for the three-dimensional GDL geometry is solved using the STATIC STRUCTURE module of commercial software ANSYS. Then, the geometry with GDL deformation is obtained and rebuilt by SolidWorks and

https://doi.org/10.1021/acsomega.3c08756
ACS Omega 2024, 9, 9383−9395

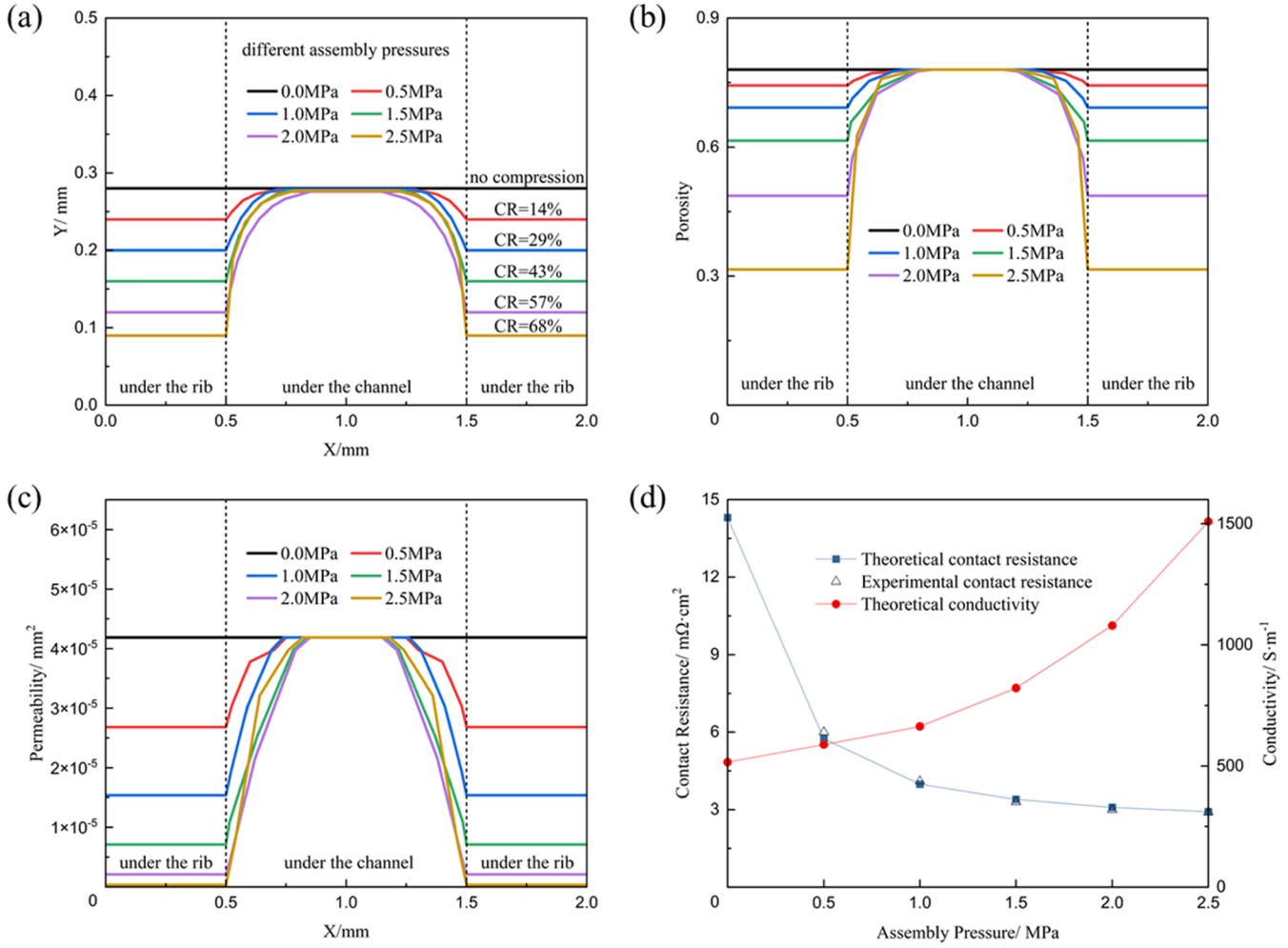

Figure 4. Deformation and physical parameters of GDL under different assembly pressures: (a) compression deformation of GDL, (b) porosity distribution after deformation, (c) permeability distribution after deformation, and (d) contact resistance and conductivity under different assembly pressures.

imported into ANSYS to remesh, providing the computation domain for the CFD simulation of fuel cells. The characteristic parameters, such as porosity and permeability of GDL after deformation, are computed by empirical formula, and the obtained data are imported into FLUENT through UDFs. The continuity and momentum equations as well as the heat transfer and charge transfer equations of the PEMFC model are solved by FLUENT. The current density is obtained for a given voltage from 1.0 to 0.3 V with steps of 0.1 V. Some of the physical parameters and basic operation case conditions used in the simulation are listed in Tables 1, 2, and 3.

For solid-mechanics calculations, the assembly load is applied to BP and the other outer contour surfaces are set as frictionless supports. Therefore, the cell can only generate displacement in the *Y*-direction, while those in the *X*- and *Z*-directions are fixed to zero.

Table 2. Mechanical Parameters of the PEMFC Components

parameters	PEM	GDL	CL	BP
density (kg·m^{-3})	1980	1000	1000	1000
Young's modulus (MPa)	232[29]	6.3[38]	249	13 000
poisson ratio	0.253	0.256[38]	0.3	0.26

Table 3. Physical Properties of the PEMFC Components

parameter	PEM	GDL	CL	BP
primary electrical conductivity (S·m^{-1})	9.825	300	300	20 000
primary porosity	0.4	0.78	0.3	0
thermal conductivity (W·m^{-1}·K^{-1})	0.95	1	1	20
specific heat capacity (J·kg^{-1}·K^{-1})	833[38]	568[30]	3300	1580[38]
thermal expansion coefficient (K)	1.23×10^{-4}	2.5×10^{-6}	3.7×10^{-5}	0.9×10^{-6}

3. RESULTS AND DISCUSSION

3.1. Grid Reliability Verification. The hexahedral grid is used to divide the single-channel model, and the reliability of grid numbers is studied. The obtained current densities at 0.4 V under assembly pressure of 1.0, 2.0, and 2.5 MPa are plotted in Figure 2, with the grid numbers from 10 080 to 308 000. The current densities increase with the grid number. After the grid number reaches 200 736, the variation of current density with the increasing grid number is below 1%. Therefore, 200 736 grids are used in this study, considering the balance between calculation time and accuracy.

https://doi.org/10.1021/acsomega.3c08756
ACS Omega 2024, 9, 9383−9395

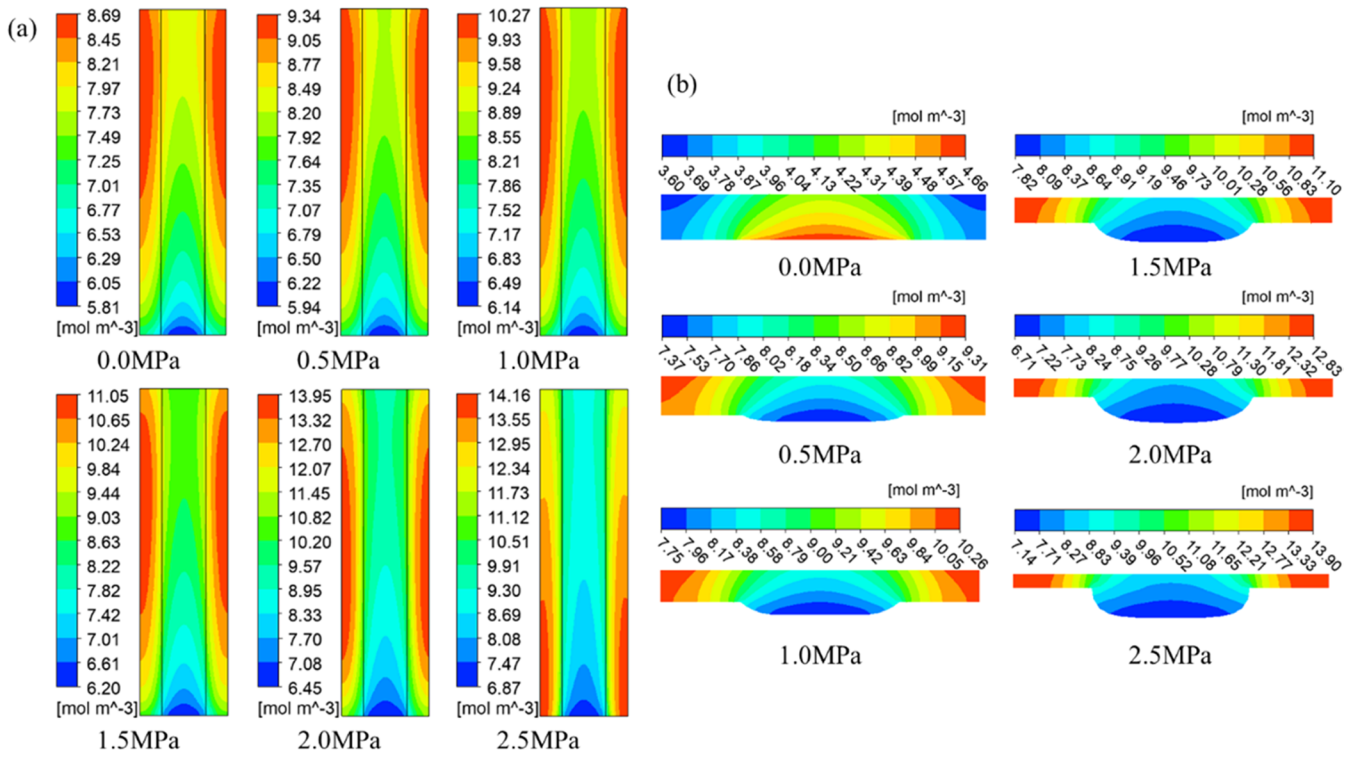

Figure 5. Distribution of molar concentration of water in the middle of cathode GDL at 0.5 V, (a) *XZ* section, and (b) *XY* section.

3.2. Experimental Verification. In order to verify the reliability of the PEMFC model and the calculation results, the polarization curve under 1.5 MPa is compared with the experimental results from the reference,[32] as shown in Figure 3. It can be clearly seen that the numerical calculation results agree well with the experimental data, which proves the reliability of the numerical simulation.

3.3. Effects of Assembly Pressures of Deformation and Characteristic Parameters of GDL. Based on the assumption that the channels and other components do not deform after compression, the structure deformation only occurs in GDL, as shown in Figure 4. The channel−rib flow field causes the nonuniform deformation of GDL. In the direction of the *X*-axis, the thickness of GDL is different in the area under the channel and rib, especially for the large assembly pressures. Then, the physical parameters such as permeability, porosity, and conductivity of deformed GDL can be calculated because they are the functions of the thickness.

The GDL deformation for various assembly pressures from 0 to 2.5 MPa is shown in Figure 4a. Comparatively, the deformation in the area under the rib is larger than that under the channel, while the deformation in the middle of the channel region is very small and neglected in this work. The thickness of GDL under the ribs decreases from primary 0.28−0.09 mm as the assembly pressure increases from 0 to 2.5 MPa. The compression ratio (CR) is defined as eq 16.[33]

$$\mathrm{CR} = \frac{\delta_{\mathrm{primary}} - \delta}{\delta_{\mathrm{primary}}} \tag{16}$$

where $\delta_{\mathrm{primary}}$ indicates the primary GDL thickness and δ indicates the thickness after compression. It can be seen from the figure that the maximum CR reaches 68% under the assembly pressure of 2.5 MPa.

The porosity and permeability of GDL also correspondingly vary with compression deformation.[31] The porosity, ε, in Figure 4b is obtained by[34]

$$\varepsilon = 1 - (1 - \varepsilon_{\mathrm{primary}})\frac{\delta_{\mathrm{primary}}}{\delta} \tag{17}$$

where $\varepsilon_{\mathrm{primary}}$ indicates the primary porosity, which is equal to 0.78 in this paper. The porosity under the rib is lower than that under the channel and decreases with the increase of assembly pressure. Meanwhile, a larger difference in porosity variation is observed under a higher assembly pressure. The difference in the porosity value varies about 4% as assembly pressure increases from 0 to 0.5 MPa, while the value reaches 17% as assembly pressure increases from 2.0 to 2.5 MPa.

The permeability, *K*, in Figure 4c is obtained by[35]

$$K = \frac{\varepsilon(\varepsilon - 0.037)^{2.661} {d_{\mathrm{f}}}^2}{8(\mathrm{In}\ \varepsilon)^2 0.975(1.661\varepsilon - 0.037)^2} \tag{18}$$

where d_{f} is the diameter of carbon fiber and is equal to 9.75 μm. With the increase of pressure, the permeability decreases continuously. The permeability value under the rib greatly changes from 4.19×10^{-5} to 3.75×10^{-7} mm^2 when the assembly pressure increases from 0 to 2.5 MPa.

The changes in contact electric resistance and conductivity under different pressures are plotted in Figure 4d. The contact electric resistance, R_{contact}, is obtained.[36]

$$R_{\mathrm{contact}} = 2.2163 + 3.5306 \cdot \frac{A_{\mathrm{contact}}}{P_{\mathrm{assembly}} \cdot A_{\mathrm{assembly}}} \tag{19}$$

where A_{contact} is the contact area of BP and GDL and P_{assembly} and A_{assembly} are the assembly pressure and the assembly area, respectively. The change in A_{contact} is ignored in this work, which is equal to 0.5 cm^2. It can be seen that the contact resistance

https://doi.org/10.1021/acsomega.3c08756
ACS Omega 2024, 9, 9383−9395

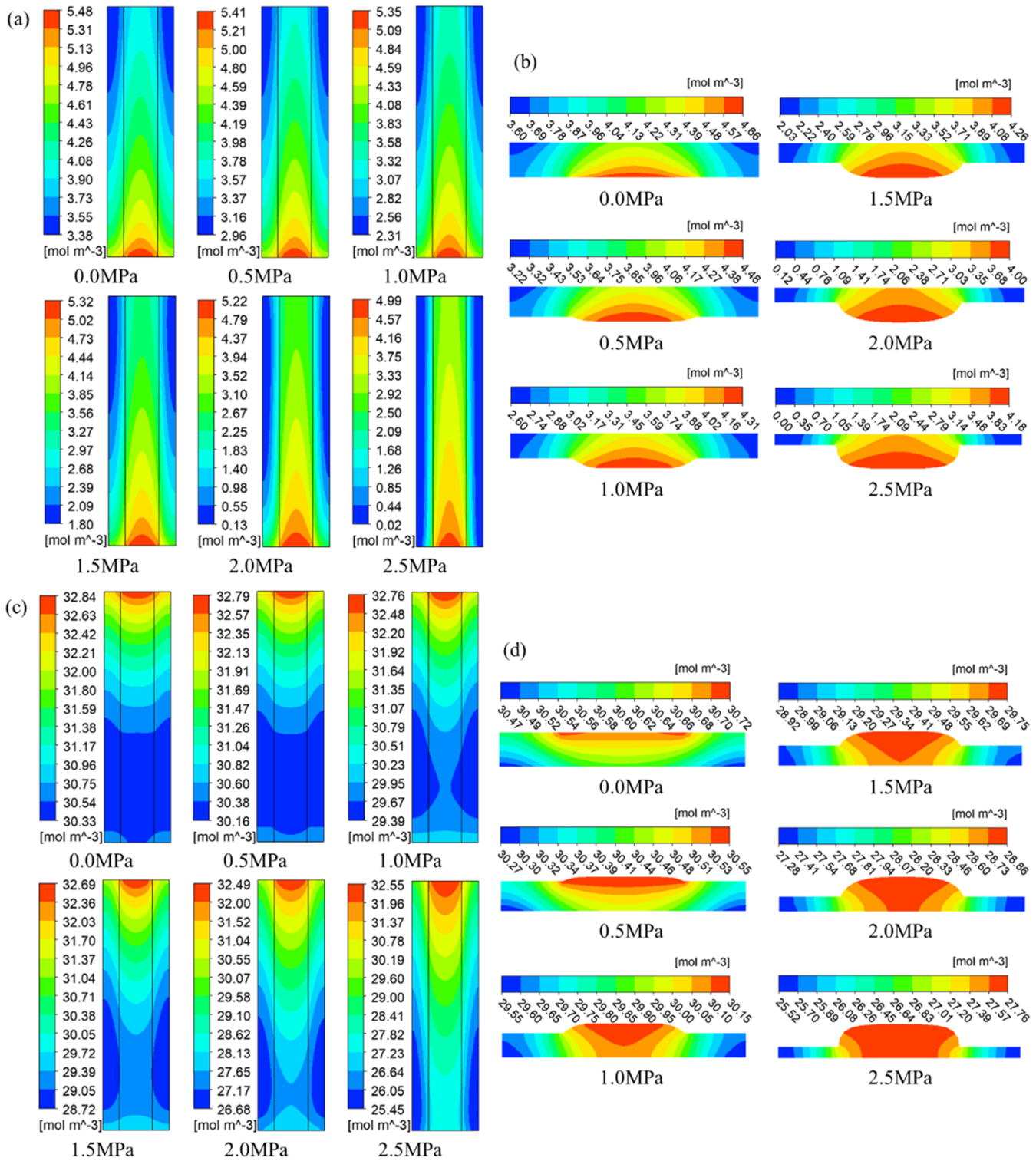

Figure 6. Oxygen distribution at (a) *XZ*-plane and (b) *XY*-plane, and hydrogen distribution at (c) *XZ*-plane and (d) *XY*-plane in the GDL under 0.5 V.

reduces as assembly pressure increases from 0 to 1.0 MPa. Then, the slope of the curve becomes small, with an electric resistance value of 2.922 mΩ·cm^2 at 2.5 MPa. The obtained contact electric resistance values are compared with the experimental results from Mishra et al.[36] It is shown that the two curves fit very well, indicating the high reliability of our simulation results.

The effective conductivity γ_{eff} of GDL in Figure 4d is obtained by[37]

$$\gamma_{eff} = \gamma_{primary}(1 - \varepsilon)^{1.5} \quad (20)$$

where $\gamma_{primary}$ indicates the primary conductivity, which is equal to 300 S·m^{-1}.

The conductivity increases from 516 to 1509 S·m^{-1} with an increase in assembly pressure. Different from the contact electric resistance curve, the slope of the conductivity curve increases with the value of assembly pressure.

https://doi.org/10.1021/acsomega.3c08756
ACS Omega 2024, 9, 9383−9395

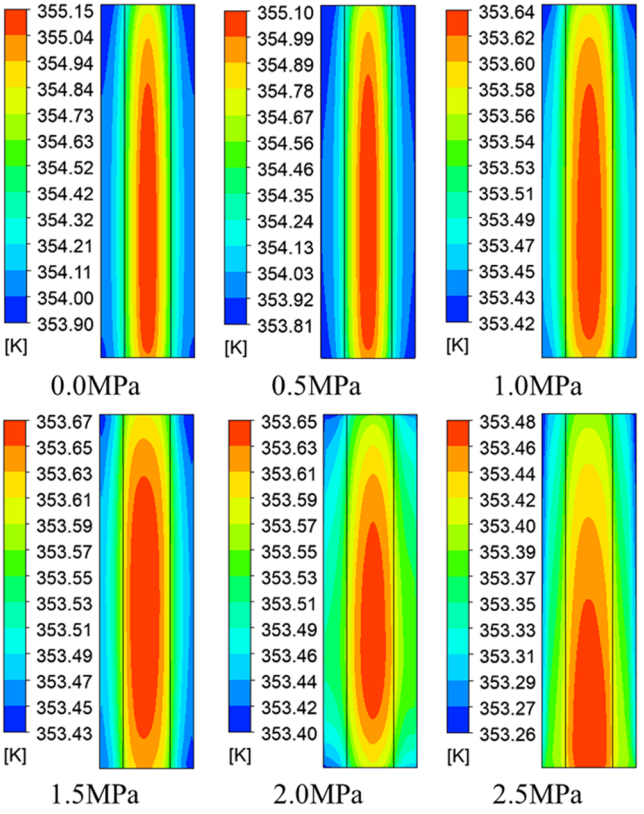

Figure 7. Temperature distribution in the middle of the proton-exchange membrane under 0.5 V.

The obtained porosity, permeability, and conductivity of GDL are imported into FLUENT by UDFs for CFD calculations for the fuel cell performance discussion.

3.4. Distribution of Water Concentration. Figure 5 shows the distribution of water concentration in the cathode GDL at the (a) *XZ*-plane and (b) *XY*-plane under different assembly pressures. It is observed that the molar concentration of water in the region below the rib is higher than that below the channel for each assembly pressure. This is because the water produced in the cathode CL is more easily carried away by the airflow in the channel. In addition, the lower porosity and permeability of GDL under the ribs after compression makes the removal of water away from the rib more difficult. Thus, the GDL region under the rib is more likely to be flooded.[38] These results are in good agreement with previous experimental results.[39−41] The average molar concentration of water in the cathode GDL increases from 7.79 to 9.63 mol·m^{-3} as the assembly pressure increases from 0 to 2.5 MPa.

3.5. Distribution of Oxygen and Hydrogen. Figure 6 shows the distribution of oxygen and hydrogen in the GDL of the cathode and anode, respectively. It can be seen that the gas concentration decreases as the assembly pressure increases; the average concentrations of oxygen and hydrogen decreased from 4.21 to 2.05 mol·m^{-3} and from 30.91 to 28.74 mol·m^{-3}, respectively; the concentrations of reactants oxygen and hydrogen in the region under the channel are higher than that under the rib. The reason is that the mass transfer of compressed GDL under the rib is greatly reduced compared to that under the channel. At the same time, the volume of the channel decreases as GDL intrudes into the channel, the velocity of the gas flow in the flow passage increases, and the convection mass transfer is enhanced.[42]

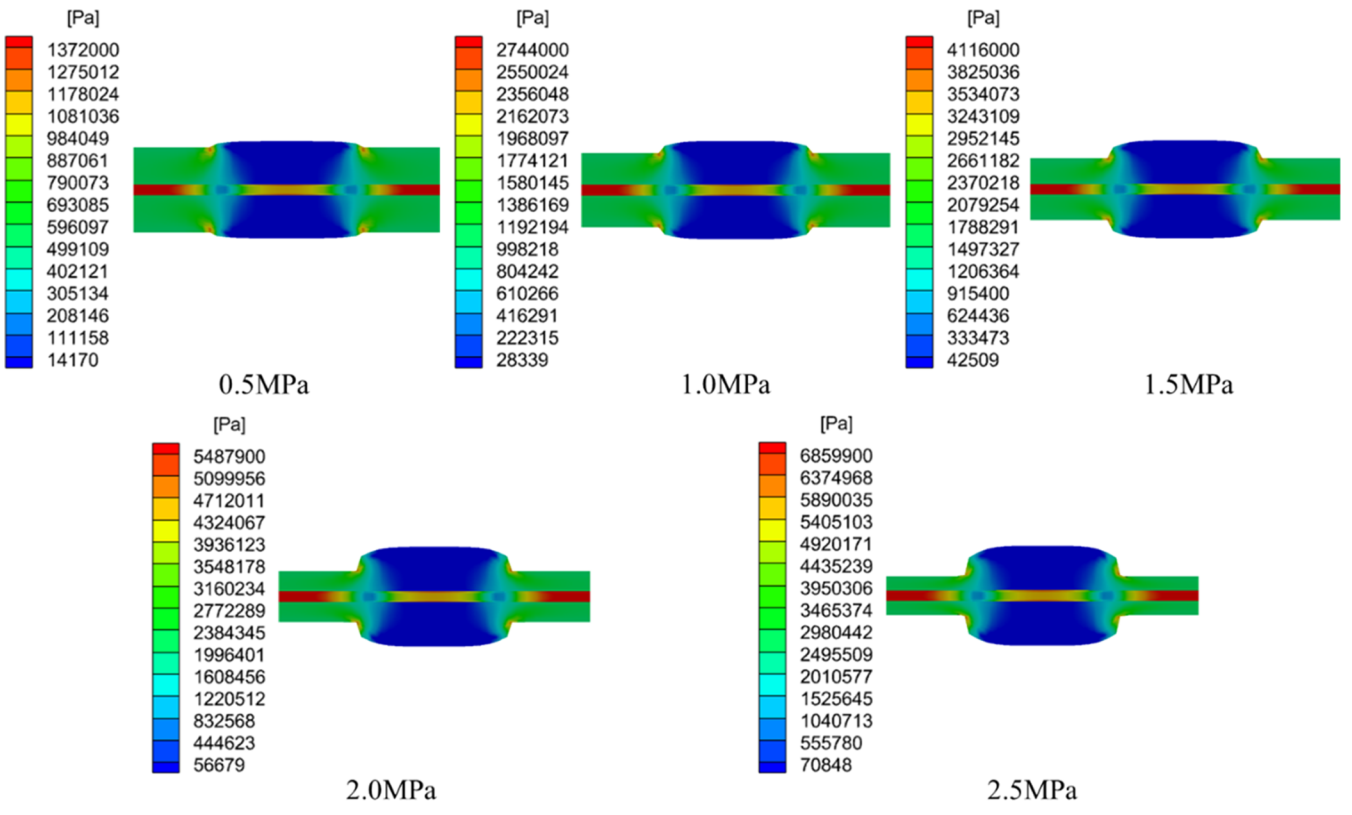

Figure 8. Mechanical stress distribution of MEA under different assembly pressures.

https://doi.org/10.1021/acsomega.3c08756
ACS Omega 2024, 9, 9383−9395

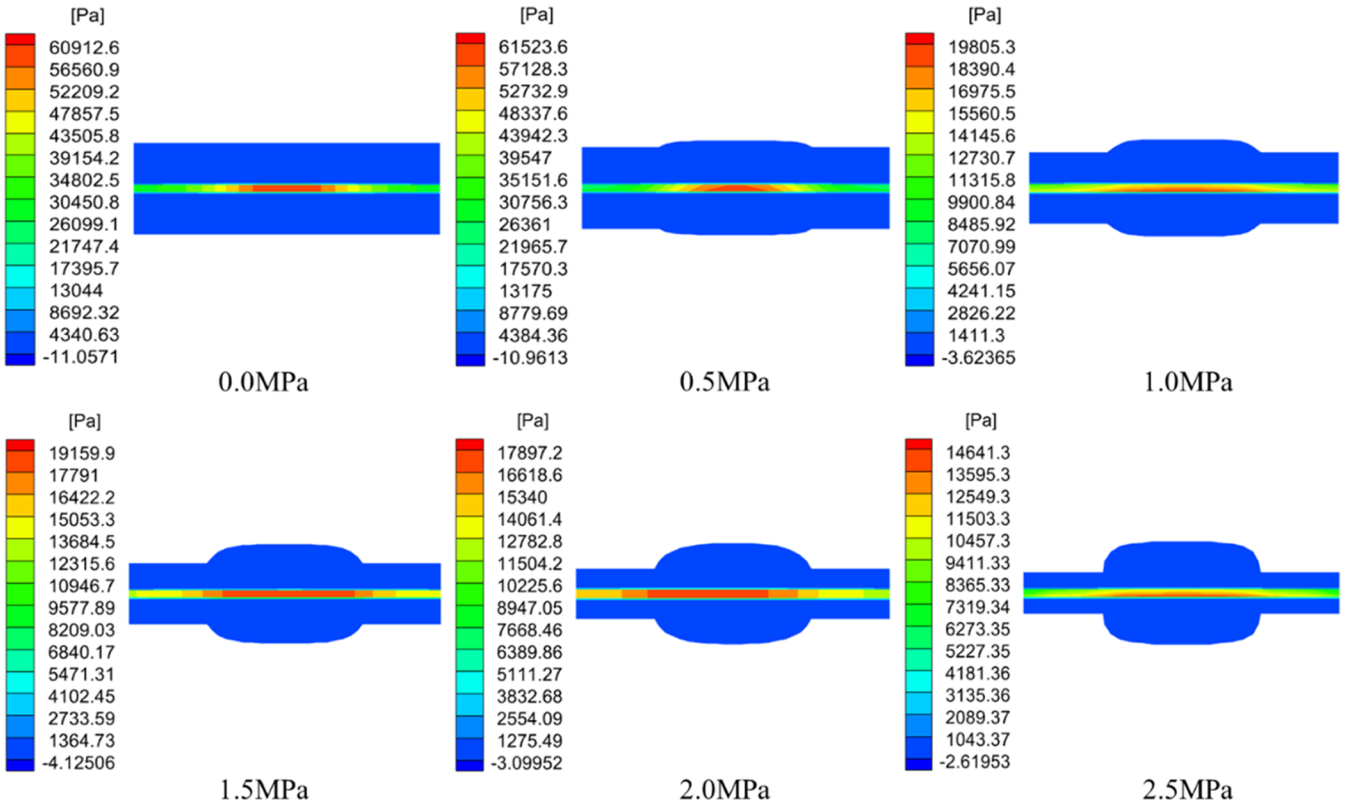

Figure 9. Thermal stress distribution of MEA under 0.5 V.

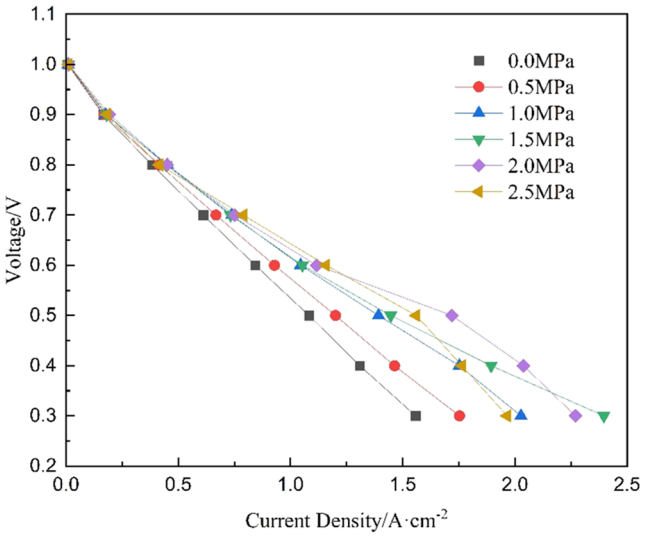

Figure 10. Performance of PEMFC under different assembly pressures.

3.6. Distribution of Temperature. Temperature has a significant effect on the PEMFC performance, especially on the proton electric resistance, gas distribution, and water content in the membrane.[43] Figure 7 illustrates the distribution of temperature at the *XZ*-plane inside the PEM under 0−2.5 MPa. The temperature of the membrane below the channel is higher than that under the rib for better mass transfer and faster reaction. With the increase of assembly pressure, the maximum temperature decreases from 355.15 to 353.48 K. This is because a higher electrical conductivity of GDL under higher assembly pressure subsequently reduces the contact electrical resistance for the neighboring components, thereby reducing the Ohmic heat.[44]

3.7. Distribution of Mechanical Stress and Thermal Stress. Figure 8 shows the distribution of mechanical stress in MEA. It indicates that the maximum stress appears in the membrane during the assembling process. The maximum value increases from 1.372 to 6.859 MPa as the assembly pressure increases from 0.5 to 2.5 MPa. The mechanical stress under the rib of PEM is obviously greater than that under the channel for the compression force coming from the rib vertically. For the GDL, the higher mechanical stress exists at the junction point of the channel and the rib because a sudden change of the assembly force leads to stress concentration.

Thermal stress is mainly generated during the operation of cells, and it affects the durability of PEMFC.[30] Thus, it is very important to study the magnitude and distribution of thermal stress in cells under different pressures. Figure 9 shows the thermal stress distribution of MEA in the PEMFC, which is obtained by[45]

$$\sigma^T = E(T - T_0)\alpha \tag{21}$$

where E indicates Young's modulus (Pa), T_0 indicates the operating temperature (K), T indicates the actual temperature (K), and α indicates the thermal expansion coefficient. It can be seen that the thermal stress appears mainly in PEM under the middle part of the channel region, while the influence is smaller in CL and GDL. This is because the thermal expansion coefficient of PEM is larger than those of CL and GDL.[30] The maximum value of the thermal stress in PEM decreases from 60912.6 to 14641.3 Pa with the increase of the assembly pressure. A more uniform distribution of thermal stress is observed under a higher assembly pressure. It is consistent with the temperature distribution as depicted in Figure 9. Higher

https://doi.org/10.1021/acsomega.3c08756
ACS Omega 2024, 9, 9383−9395

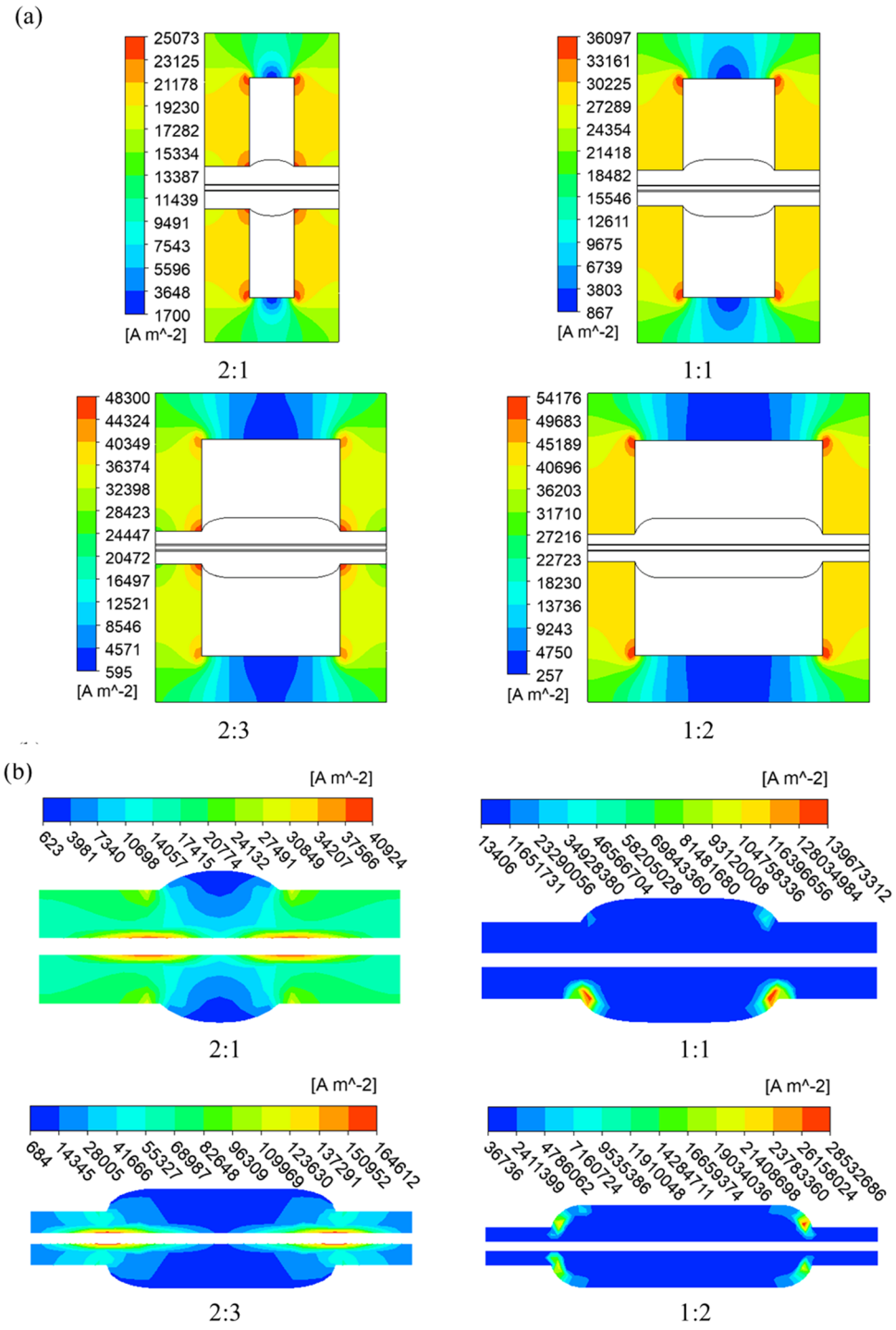

Figure 11. Current density distribution at z = 25 mm plane for different rib−channel ratios with assembly pressure of 1.5 MPa and operating voltage of 0.5 V (a) in BP and (b) GDL.

stress values, both mechanical and thermal stress, were found in the membrane. While the maximum mechanical stress is 6.8599 MPa, obtained at 25 MPa, the maximum thermal value is only 61523.6 Pa at 0.5 MPa.

3.8. Performance of PEMFC. Figure 10 plots the performance of PEMFC under different assembly pressures. Results show that the current density at 0.3 V increases from 0 to 1.5 MPa and then decreases from 20 to 25 MPa. The highest values, 2.397 and 2.271 A·cm^{-2}, are obtained at 1.5 and 2.0 MPa. The performance increases with the pressure increase and then decreases as the assembly continuously increases. There is an obvious mass transfer limit around voltage 0.5 V for the high assembly pressure due to the big compression effect. On the one hand, lower contact electric resistance and higher conductivity of GDL obtained under high pressure can reduce the internal electric resistance and contact electric resistance. On the other hand, mass transfer reduces the porosity and permeability of GDL with decreasing assembly pressure. Therefore, the optimized cell performance at 1.5−2.0 MPa is a result of the balance of both the effects.

3.9. Rib−Channel Ratio Effect. The rib−channel ratios affect the transportation phenomenon and cell performance of

https://doi.org/10.1021/acsomega.3c08756
ACS Omega 2024, 9, 9383−9395

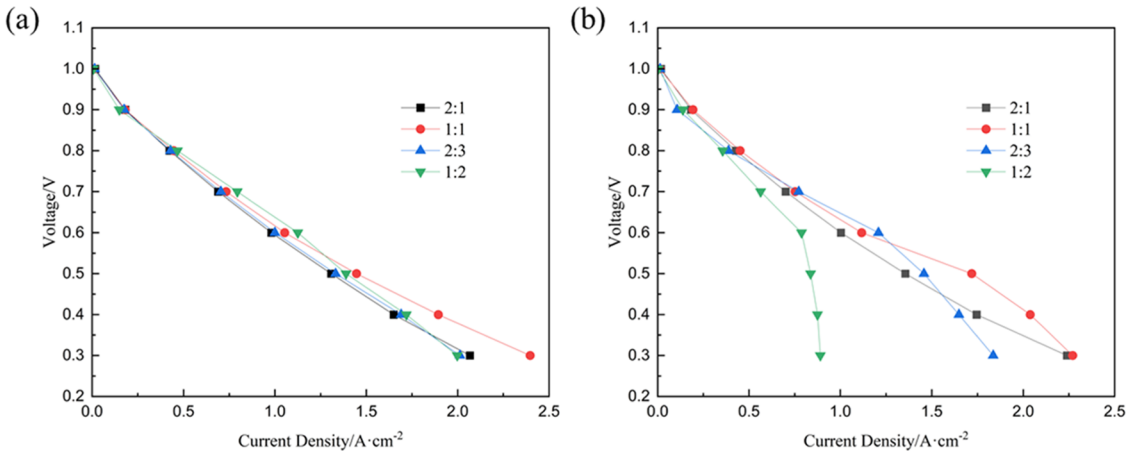

Figure 12. Polarization performance of PEMFC with different rib−channel ratios at (a) 1.5 and (b) 2.0 MPa.

the PEMFC by changing the passages of fluid flow and charge transfer. The rib width is fixed at 0.5 mm, and the channel width varies from 0.25 to 1 mm to obtain rib−channel ratios of 2:1, 1:1, 2:3, and 1:2 and study the effect of rib−channel ratios on cell performance.

Figure 11 shows the current density distribution at the $z = 25$ mm plane for different rib−channel ratios with an assembly pressure of 1.5 MPa and an operating voltage of 0.5 V. It can be observed from Figure 11a that under different assembly pressures, the distribution of current density is generally similar. The highest current density is found at the corners of the current collector, while the lowest current density is observed in the middle position at the top and bottom of the current collector. The reason for this phenomenon is that the electrons in the GDL below the channel move to the closest point of the current collector and lots of electrons aggregate over there; channels do not conduct electric current, and the current collector at the top of the channel is larger than that in other places. Furthermore, the maximum current density increases with increasing assembly pressure, which means the higher aggregation effect of electrons. In Figure 11b, it is found that for the 2:1 and 2:3 models, the maximum current density appears below the junction position of the ribs and channels and close to the PEM. For the 1:1 and 1:2 models, the maximum current density occurs near the connection position of GDL, rib, and channel.

The effects of rib−channel ratios (2:1, 1:1, 2:3, 1:2) on the cell performances are shown in Figure 12. In Figure 12a, it is observed that the flow field with a 1:1 rib−channel ratio has the highest current density at 0.3 V under 1.5 MPa. In addition, a higher current density at 0.3 V is obtained by the flow field with a ratio of 1:1 under 20 MPa, as shown in Figure 12b. While an obvious concentration polarization is found for the flow field with a ratio of 2:3 and 1:2, the current density shows a downward trend at a high current density. Therefore, the optimum rib−channel ratio is 1:1 under both the assembly pressures of 1.5 and 2.0 MPa.

4. CONCLUSIONS

The effect of assembly pressure on GDL deformation is investigated using FEM. Based on the deformed GDL and its variable physical properties, the 3D PEMFC model is developed and computed to elucidate the transportation phenomena and cell performance by commercial software Ansys Fluent with UFDs. The following are some main research results:

(1) The porosity and permeability of GDL decrease after compression, in particular in the region under the rib, which hinders the mass transfer performances, including the accumulation of more water and a lower gas concentration.

(2) GDL compression results in higher conductivity and lower contact electric resistance between GDL and BP, which reduces the ohmic electric resistance and decreases the internal temperature of the cell.

(3) The mechanical stress increases with the increase of assembly pressure, and the thermal stress decreases with the increase of assembly pressure.

(4) The maximum current density at 0.3 V is obtained under 1.5 and 2.0 MPa due to the trade-off between mass transfer resistance and ohmic resistance.

(5) Under the assembly pressures of 1.5 and 2.0 MPa, the flow field with the rib−channel ratio of 1:1 has the highest current density at 0.3 V.

AUTHOR INFORMATION

Corresponding Author

Guilin Hu − *School of Mechanical and Energy Engineering, Zhejiang University of Science and Technology, Hangzhou 310023, China;* orcid.org/0000-0001-6703-9135; Email: enehgl@163.com

Authors

Hangwei Lei − *School of Mechanical and Energy Engineering, Zhejiang University of Science and Technology, Hangzhou 310023, China*

Yuzhen Xia − *School of Mechanical and Energy Engineering, Zhejiang University of Science and Technology, Hangzhou 310023, China*

Complete contact information is available at: https://pubs.acs.org/10.1021/acsomega.3c08756

Notes

The authors declare no competing financial interest.

ACKNOWLEDGMENTS

This work was supported by Zhejiang Provincial Outstanding Youth Fund (R1100065) and Hangzhou Lingfei Technology Co., Ltd.

REFERENCES

(1) Lu, J.; Xia, Y.; Hu, Y.; Wang, Z.; Lei, H.; Hu, G. Study on transport phenomena and performance of proton exchange membrane fuel cell with radial flow fields. *Eng. Appl. Comput. Fluid Mech.* **2023**, *17* (1), No. 2156925.

(2) Jiao, K.; Xuan, J.; Du, Q.; Bao, Z.; Xie, B.; Wang, B.; Zhao, Y.; Fan, L.; Wang, H.; Hou, Z.; Huo, S.; Nigel, P.; Yin, Y.; Michael, D. Designing the next generation of proton-exchange membrane fuel cells. *Nature* **2021**, *595* (7867), 361−369.

(3) Niu, Z.; Jiao, K.; Wang, Y.; Du, Q.; Yin, Y. Numerical simulation of two-phase cross flow in the gas diffusion layer microstructure of proton exchange membrane fuel cells. *Int. J. Energy Res.* **2018**, *42* (2), 802−816.

(4) Bao, N.; Zhou, Y.; Zhou, Y.; Yin, Y.; Du, Q.; Chen, J. Effect of gas diffusion layer deformation on liquid water transport in proton exchange membrane fuel cell. *Eng. Appl. Comput. Fluid Mech.* **2014**, *8* (1), 26−43, DOI: 10.1080/19942060.2014.11015495.

(5) Bernardi, D. M.; Verbrugge, M. W. A mathematical model of the solid-polymer-electrolyte fuel cell. *J. Electrochem. Soc.* **1992**, *139*, 2477−2491.

(6) Chen, H.; Guo, H.; Ye, F.; Ma, C. F. A numerical study of baffle height and location effects on mass transfer of proton exchange membrane fuel cells with orientated-type flow channels. *Int. J. Hydrogen Energy* **2021**, *46* (1−2), 7528−7545.

(7) Yu, Y.; Zhang, Z. G.; He, L. Y.; Yang, X. X.; Wan, X. B.; Sui, P. C.; Pan, M. Effects of distribution zone design on flow uniformity and pressure drop in PEMFC. *J. Electrochem. Soc.* **2021**, *168* (9), No. 094505.

(8) Zhang, Z. Q.; Liu, W.; Wang, Y. L. Three dimensional two-phase and non-isothermal numerical simulation of multi-channels PEMFC. *Int. J. Hydrogen Energy* **2019**, *44*, 379−388.

(9) Ding, Y. J.; Xu, L. F.; Zheng, W. B.; Hu, Z. Y.; Shao, Y. B.; Li, J. Q.; Ouyang, M. G. Characterizing the two-phase flow effect in gas channel of proton exchange membrane fuel cell with dimensionless number. *Int. J. Hydrogen Energy* **2023**, *48* (13), 5250−5265.

(10) Franz, T.; Papakonstantinou, G.; Sundmacher, K. Transient hydrogen crossover in dynamically operated PEM water electrolysis cells - A model-based analysis. *J. Power Sources* **2023**, *559*, No. 232582.

(11) Huang, Z. Y.; Shen, J.; Chan, S. H.; Tu, Z. K. Transient response of performance in a proton exchange membrane fuel cell under dynamic loading. *Energy Convers. Manage.* **2020**, *226*, No. 113492.

(12) Liu, H.; Chen, J.; Hissel, D.; Hou, M.; Shao, Z. G. A multi-scale hybrid degradation index for proton exchange membrane fuel cells. *J. Power Sources* **2019**, *437*, No. 226916.

(13) Hou, Y. Z.; Li, X.; Du, Q.; Jiao, K.; Zamel, N. Pore-scale investigation of the effect of micro-porous layer on water transport in proton exchange membrane fuel cell. *J. Electrochem. Soc.* **2020**, *167* (14), No. 144504.

(14) Huang, T. M.; Huang, J.; Feng, M. C.; Yi, D. X.; Chen, X.; Ou, C. J.; Zhang, J.; Zhang, Y.; Wan, Z. M. Optimization of the thickness of catalytic layer for HT-PEMFCs based on genetic algorithm. *Energy Rep.* **2022**, *8*, 12905−12915.

(15) KP, V. B.; Varghese, G.; Joseph, T. V.; Chippar, P. Optimization of graded catalyst layer to enhance uniformity of current density and performance of high temperature-polymer electrolyte membrane fuel cell. *Int. J. Hydrogen Energy* **2022**, *47* (6), 4018−4032, DOI: 10.1016/j.ijhydene.2021.11.006.

(16) Zhu, L. J.; Zhnag, H.; Xiao, L. S.; Bazylak, A.; Gao, X.; Sui, P. C. Pore-scale modeling of gas diffusion layers: Effects of compression on transport properties. *J. Power Sources* **2021**, *496*, No. 229822.

(17) Bao, Y. Y.; Wang, Z. Z.; Gan, Y. X. Numerical investigation of compressive stress and wettability effects on fluid transport in polymer electrolyte membrane fuel cell porous layers. *Energy Technol.* **2022**, *10* (12), No. 2201028.

(18) Song, K.; Wang, Y. M.; Ding, Y. H.; Xu, H. J.; Mueller-Welt, P.; Stuermlinger, T.; Bause, K.; Ehrmann, C.; Weinmann, H. W.; Schaefer, J.; Fleischer, J.; Zhu, K.; Weihard, F.; Trostmann, M.; Schwartze, M.; Albers, A. Assembly techniques for proton exchange membrane fuel cell stack: A literature review. *Renewable Sustainable Energy Rev.* **2022**, *153*, No. 111777.

(19) Zhou, X.; Niu, Z. A.; Li, Y. N.; Sun, X. Y.; Du, Q.; Xuan, J.; Jiao, K. Investigation of two-phase flow in the compressed gas diffusion layer microstructures. *Int. J. Hydrogen Energy* **2019**, *44* (48), 26498−26516.

(20) Zhang, Z.; He, P.; Dai, Y. J.; Jin, P. H.; Tao, W. Q. Study of the mechanical behavior of paper-type GDL in PEMFC based on microstructure morphology. *Int. J. Hydrogen Energy* **2020**, *45* (53), 29379−29394.

(21) Chen, Y. Q.; Zhao, J. H.; Jin, C. H.; Ke, Y. C.; Li, D. C.; Wang, Z. X. Effect of clamping compression on the mechanical performance of a carbon paper gas diffusion layer in polymer electrolyte membrane fuel cells. *Membranes* **2022**, *12* (7), 645.

(22) Chi, P. H.; Chan, S. H.; Weng, F. B.; Su, A. Y.; Sui, P. C.; Djilali, N. On the effects of non-uniform property distribution due to compression in the gas diffusion layer of a PEMFC. *Int. J. Hydrogen Energy* **2010**, *35* (7), 2936−2948.

(23) Su, Z. Y.; Liu, C. T.; Chang, H. P.; Li, C. H.; Huang, K. J.; Sui, P. C. A numerical investigation of the effects of compression force on PEM fuel cell performance. *J. Power Sources* **2008**, *183* (1), 182−192.

(24) Chippar, P.; Kyeongmin, O.; Kang, K.; Ju, H. A numerical investigation of the effects of GDL compression and intrusion in polymer electrolyte fuel cells (PEFCs). *Int. J. Hydrogen Energy* **2012**, *37* (7), 6326−6338, DOI: 10.1016/j.ijhydene.2011.04.154.

(25) Shrivastava, N. K.; Chatterjee, A.; Harris, T. A. L. Effect of cell compression on the performance of a non−hot-pressed MEA for PEMFC. *Int. J. Energy Res.* **2020**, *44* (1), 370−387.

(26) Movahedi, M.; Ramiar, A.; Ranjber, A. A. 3D numerical investigation of clamping pressure effect on the performance of Proton Exchange Membrane fuel cell with interdigitated flow field. *Energy* **2018**, *142*, 617−632.

(27) Kang, H.; Zhan, Z. G.; Yang, X. F.; Zhang, Z. B.; Shi, J. R.; Jiang, P. X.; Pan, M. Numerical Study on the Stress Concentration Phenomenon in the Membranes of PEMFCs in an Assembled State. *Int. J. Hydrogen Energy* **2020**, *146* (5), No. 04020053.

(28) Li, W.; Yang, W.; Zhang, W.; Qu, Z.; He, Y. Three-dimensional modeling of a PEMFC with serpentine flow field incorporating the impacts of electrode inhomogeneous compression deformation. *Int. J. Hydrogen Energy* **2019**, *44* (39), 22194−22209.

(29) Hu, G.; Ji, C.; Xia, Y.; Suo, Y.; Wu, X.; Zhang, Z. Assembly mechanics and its effect on performance of proton exchange membrane fuel cell. *Int. J. Electrochem. Sci.* **2019**, *14* (2), 1358−1371.

(30) Oh, K.; Chippar, P.; Ju, H. Numerical study of thermal stresses in high temperature proton exchange membrane fuel cell (HT-PEMFC). *Int. J. Hydrogen Energy* **2014**, *39* (6), 2785−2794.

(31) Xia, Y.; Hu, Y.; Hu, G.; Lei, H.; Lu, J.; Wang, Z.; Wang, Q. Numerical analysis on the effects of manifold design on flow uniformity in a large proton exchange membrane fuel cell stack. *Int. J. Hydrogen Energy* **2023**, *48*, 5643−5655.

(32) Corda, G.; Fontanesi, S.; d'Adamo, A. Methodology for PEMFC CFD Simulation Including the Effect of Porous Parts Compression. *Int. J. Hydrogen Energy* **2022**, *47* (32), 14658−14673.

(33) Zhang, H.; Xiao, L.; Chuang, P.; Djilali, N.; Sui, P. Coupled stress-strain and transport in proton exchange membrane fuel cell with metallic bipolar plates. *Appl. Energy* **2019**, *251*, No. 113316.

(34) Jiao, K.; Park, J.; Li, X. Experimental investigations on liquid water removal from the gas diffusion layer by reactant flow in a PEM fuel cell. *Appl. Energy* **2010**, *87* (9), 2770−2777.

(35) Tomadakis, M. M.; Robertson, T. J. Viscous permeability of random fiber structures: comparison of electrical and diffusional estimates with experimental and analytical results. *J. Compos. Mater.* **2005**, *39* (2), 163−188, DOI: 10.1177/0021998305046438.

(36) Mishra, V.; Yang, F.; Pitchumani, R. Measurement and prediction of electrical contact resistance between gas diffusion layers and bipolar plate for applications to PEM fuel cells. *J. Fuel Cell Sci. Technol.* **2004**, *1* (1), 2−9.

(37) Das, P. K.; Li, X.; Liu, Z. S. Effective transport coefficients in PEM fuel cell catalyst and gas diffusion layers: Beyond Bruggeman approximation. *Appl. Energy* **2010**, *87* (9), 2785−2796.

(38) Zhou, Y.; Jiao, K.; Du, Q.; Yin, Y.; Li, X. Gas diffusion layer deformation and its effect on the transport characteristics and

https://doi.org/10.1021/acsomega.3c08756
ACS Omega 2024, 9, 9383−9395

performance of proton exchange membrane fuel cell. *Int. J. Hydrogen Energy* **2013**, *38* (29), 12891−12903.
(39) Iranzo, A.; Boillat, P. Liquid water distribution patterns featuring back-diffusion transport in a PEM fuel cell with neutron imaging. *Int. J. Hydrogen Energy* **2014**, *39* (30), 17240−17245.
(40) Wang, Y.; Chen, K. S. Effect of spatially-varying GDL properties and land compression on water distribution in PEM fuel cells. *J. Electrochem. Soc.* **2011**, *158* (11), B1292.
(41) Owejan, J.; Trabold, T.; Jacobson, D.; Baker, D.; Hussey, D.; Arif, M. In situ investigation of water transport in an operating PEM fuel cell using neutron radiography: Part 2 − Transient water accumulation in an interdigitated cathode flow field. *Int. J. Heat Mass Transfer* **2006**, *49* (25), 4712−4720.
(42) Taymaz, I.; Benli, M. Numerical study of assembly pressure effect on the performance of proton exchange membrane fuel cell. *Energy* **2010**, *35* (5), 2134−2140.
(43) Toghyani, S.; Nafchi, F.; Afshari, E.; Hasanpour, K.; Baniasadi, E.; Atyabi, S. Thermal and electrochemical performance analysis of a proton exchange membrane fuel cell under assembly pressure on gas diffusion layer. *Int. J. Hydrogen Energy* **2018**, *43* (9), 4534−4545.
(44) Kulkarni, N.; Cho, J.; Jervis, R.; Roberts, E.; Francesco, I.; Kok, M.; Shearing, P.; Brett, D. The effect of non-uniform compression on the performance of polymer electrolyte fuel cells. *J. Power Sources* **2022**, *521*, No. 230973.
(45) Tang, Y.; Santare, M.; Karlsson, A.; et al. Stresses in proton exchange membranes due to hygro-thermal loading. *J. Fuel Cell Sci. Technol.* **2006**, *3* (2), 119−124.

https://doi.org/10.1021/acsomega.3c08756
ACS Omega 2024, 9, 9383−9395